

Research Report Summary

This document represents the final report for the AFOSR FA9550-07-1-0179 research program, carried out by M. De Graef and graduate students Jeremiah MacSleyne and Patrick Callahan during the period from April 1st, 2008 until September 30th, 2010, at Carnegie Mellon University (Department of Materials Science and Engineering). During this period, the following objectives were achieved:

- we have successfully applied 3-D moment invariant analysis to several experimental data sets;
- we have extended 2-D moment invariant analysis to include up to 12th order moments;
- we have initiated the study of higher order moment invariants (3rd and 4th orders) in 3-D;
- we have concluded the optimization of an image registration algorithm employing the concept of mutual information;
- we have applied the moment invariant approach to synthetically generated microstructures.

The results of this work were presented at several conferences and invited seminars:

- *Moment Invariant Shape Descriptors for 2-D and 3-D Microstructure Representation*, J. MacSleyne, J. Simmons and M. De Graef; International Conference on the Texture of Materials (ICOTOM), Pittsburgh, June 2008.
- *Integration of Focused Ion Beam Serial Sectioning and Orientation Imaging Microscopy for 3-D Microstructure Reconstruction in a Ni-base Superalloy*, M. De Graef; International Conference on the Texture of Materials (ICOTOM), Pittsburgh, June 2008.
- *Representation and Reconstruction of Three-Dimensional Microstructures in Ni-based Superalloys*, M. De Graef; AFOSR Program Review, Washington DC, 6/16/08;
- *From 2-D observations to 3-D microstructures: an overview of recent advances*, M. De Graef, Departmental Seminar, Department of Materials Science and Engineering, University of Michigan, 11/21/08 (invited);
- *From 2-D observations to 3-D microstructures: an overview of recent advances*, M. De Graef, Catholic University of Leuven, Belgium, 1/16/09 (invited);
- *3-D moment invariants for the description of precipitate morphology and evolution in nickel based superalloys*, J. MacSleyne and M. De Graef, TMS Annual Meeting, San Francisco, CA, 2/17/09;
- *Turning 2-D images into 3-D data stacks: recent advances*, M. De Graef, University of Antwerp, Belgium, 3/9/09 (invited);

Report Documentation Page			Form Approved OMB No. 0704-0188		
Public reporting burden for the collection of information is estimated to average 1 hour per response, including the time for reviewing instructions, searching existing data sources, gathering and maintaining the data needed, and completing and reviewing the collection of information. Send comments regarding this burden estimate or any other aspect of this collection of information, including suggestions for reducing this burden, to Washington Headquarters Services, Directorate for Information Operations and Reports, 1215 Jefferson Davis Highway, Suite 1204, Arlington VA 22202-4302. Respondents should be aware that notwithstanding any other provision of law, no person shall be subject to a penalty for failing to comply with a collection of information if it does not display a currently valid OMB control number.					
1. REPORT DATE 20 DEC 2010		2. REPORT TYPE		3. DATES COVERED	
4. TITLE AND SUBTITLE Representation and Reconstruction of Three-dimensional Microstructures in Ni-based Superalloys			5a. CONTRACT NUMBER FA9550-07-1-0179		
			5b. GRANT NUMBER		
			5c. PROGRAM ELEMENT NUMBER		
6. AUTHOR(S) Marc De Graef			5d. PROJECT NUMBER		
			5e. TASK NUMBER		
			5f. WORK UNIT NUMBER		
7. PERFORMING ORGANIZATION NAME(S) AND ADDRESS(ES) Carnegie Mellon University, 5000 Forbes Avenue, Pittsburgh, PA, 15213-3890			8. PERFORMING ORGANIZATION REPORT NUMBER Oracle # 1150061		
9. SPONSORING/MONITORING AGENCY NAME(S) AND ADDRESS(ES)			10. SPONSOR/MONITOR'S ACRONYM(S)		
			11. SPONSOR/MONITOR'S REPORT NUMBER(S)		
12. DISTRIBUTION/AVAILABILITY STATEMENT Approved for public release; distribution unlimited.					
13. SUPPLEMENTARY NOTES					
14. ABSTRACT We have applied the theory of 3-D moment invariants to a variety of shapes, including experimental serial sectioning data sets and synthetically generated microstructures. The method is easy to use, and allows for a quantitative description of shapes. Further applications of this approach are currently being considered, including extension to higher order moment invariants.					
15. SUBJECT TERMS					
16. SECURITY CLASSIFICATION OF:			17. LIMITATION OF ABSTRACT	18. NUMBER OF PAGES 31	19a. NAME OF RESPONSIBLE PERSON
a. REPORT unclassified	b. ABSTRACT unclassified	c. THIS PAGE unclassified			

- *Towards a quantitative comparison between experimental and synthetic microstructures*, Patrick Callahan, M. Groeber, and M. De Graef; MS& T, Pittsburgh, October 2009.
- *From 2-D observations to 3-D microstructures: an overview of recent advances*, M. De Graef, University of Antwerp, Belgium, April 2009.
- *Beyond the spherical cow: a shape-first approach to modeling physical quantities*, M. De Graef, FZU, Czech Republic, September 2009.
- *Using moment invariants to assess the realism of digitally constructed microstructures*, P. Callahan, M. Groeber, and M. De Graef, TMS Annual meeting, Seattle, February 2010.

Furthermore, the following papers were published or submitted:

- *On the Use of Moment Invariants for the Automated Analysis of 3-D Particle Shapes*, J. MacSleyne, J. Simmons and M. De Graef, Modeling and Simulations in Materials Science and Engineering, **16**, 045008 (2008).
- *On the use of moment invariants for the automated classification of 3-D particle shapes*, J. MacSleyne, J.P. Simmons and M. De Graef, Modeling and Simulations in Materials Science and Engineering, **16**, 045008 (2008)
- *On the Use of 2-D Moment Invariants for the Automated Classification of Particle Shapes*, J. MacSleyne, J. Simmons and M. De Graef, Acta Materialia, **56**, pp. 427-437 (2009);
- *Application of joint histogram and mutual information to registration and data fusion problems in serial sectioning microstructure studies*, E.B. Gulsoy, J.P. Simmons, and M. De Graef, Scripta Materialia, **60**, 381-384, (2009);
- *Application and Further Development of Advanced Image Processing Algorithms for Automated Analysis of Serial Section Image Data*, J.P. Simmons, P. Chuang, M.L. Comer, M. Uchic, J.E. Spowart, and M. De Graef, ””, Modelling and Simulations in Materials Science and Engineering, **17**, 025002 (2009)
- M.D. Uchic, M. De Graef, R. Wheeler, and D.M. Dimiduk, “Microstructural tomography of a Ni₇₀Cr₂₀Al₁₀ superalloy using focused ion beam microscopy,” *Ultramicroscopy*, vol. 109, pp. 1229-1235 (2009).
- J.P. MacSleyne, M.D. Uchic, J.P. Simmons, and M. De Graef, “Three-dimensional analysis of secondary γ' precipitates in Rene-88 DT and UMF-20 superalloys,” *Acta Materialia*, vol. 57, pp. 6251-6267 (2009).

The following pages describe briefly the most important findings.

I Moment invariants in 3-D

We have derived a theoretical model for the 3-D moment invariants of second order. These are three numbers, represented by the symbols $0 \leq \bar{\Omega}_i \leq 1$ ($i = 1, 2, 3$), which are computed starting from the shape of an object. The moment invariants are invariant with respect to either similarity or affine coordinate transformations, which renders them particularly useful as quantitative shape descriptors that are independent of the reference frame used to represent the object(s). We have applied the moment invariant approach to the analysis of (a) secondary γ' precipitate shapes in two Ni-based superalloys, and (b) synthetically reconstructed microstructures. The following subsections summarize a few of the highlights of this research.

I.I Application to secondary γ' precipitates in Ni-based superalloys

Focused ion beam serial sectioning was used to study the 3-D morphology of secondary γ' precipitates in two nickel-based superalloys: René-88 DT, a turbine disk alloy, and UMF-20, an experimental alloy. The precipitate morphology was reconstructed from serial section images using a multi-step image processing approach, including registration, intensity corrections, segmentation, and segmentation cleanup. A total of 260 dendritic secondary γ' precipitates were obtained for the René-88 DT alloy, and 477 cuboidal precipitates in the UMF-20 alloy.

Ni	Co	Cr	Mo	W	Al	Ti	Nb	C	B
Bal.	13	16	4	4	2.1	3.7	0.7	0.03	0.015

Table 1: René-88 DT nominal alloy composition [wt. %]

René-88 DT (Damage Tolerant) is a highly alloyed polycrystalline nickel-base superalloy, produced by powder metallurgy, and commonly used in turbine disks. René-88 DT has a γ' volume fraction of around 42 % (for the standard heat treatment), a low positive lattice mismatch (0.05%), and a γ' solvus at 1130°C [1]. The chemistry is listed in Table 1. The standard heat treatment is a one hour solution treatment at 1150°C followed by a delayed oil quench and aging for eight hours at 760°C [1].

Ni	Al	Ru	Ta	Re	W	Co	Cr
Bal.	6.0	5.7	8.1	4.5	3.0	2.4	6.7

Table 2: Composition in wt. % of the UM-F20 alloy [2].

The UMF-20 alloy examined in this study is an experimental Re-containing nickel-base superalloy with high Re and Co content, and a negative lattice mismatch between the γ' precipitates and the γ matrix phase [3]. The sample was provided in the as-cast condition and the chemical composition is listed in Table 2. This alloy has liquidus and solidus temperatures of 1400°C and

1366°C, resp. [2]; additional alloy information can be found in [3–5]. The sample examined underwent a standard heat treatment, with a solution treatment for twelve hours at 1300°C, followed by aging at 1100°C for ten hours, and a water quench.

Before the γ' precipitate shapes can be analyzed quantitatively, the experimental 2-D sections must be converted to 3-D volume data sets. This conversion consists of four steps:

- image registration;
- correction for intensity shifts and fluctuations;
- image segmentation;
- post-segmentation processing.

We have developed algorithms to carry out all the above steps. These algorithms lead to a 3-D segmented (binary) stack, i.e., a stack in which each voxel is assigned a value of 0 (for the γ matrix) or 1 (for the γ' precipitates). Such a binary stack can be used in a variety of microstructure-based modeling algorithms, such as the Fourier space framework of Lebensohn [6] or the two-point statistics approach of Fullwood et al. [7]. For visualization purposes, however, the 3-D stacks are too voxelated to be rendered directly, and they must be turned into a surface representation in terms of triangular surface elements. There are many algorithms available for surface extraction, and for the present work we have used a Marching Cubes algorithm described by Lorensen and Cline [8]. The surface triangulations were stored in the Stereolithography file format (STL) and rendered using the public domain package *Paraview* [9].

For the René-88 DT data set, the final 3-D stack had dimensions of $9.5 \times 6.8 \times 3.1 \mu\text{m}^3$ and a total of 260 γ' precipitates were contained within this volume. For the UMF-20 data set, the resulting stack had dimensions of $10.5 \times 10.0 \times 4.3 \mu\text{m}^3$ and contained a total of 477 γ' precipitates. Fig. I(a) shows a 3-D rendering of all 260 γ' precipitates in the René-88 DT data set, and Fig. I(b) the corresponding microstructure for the UMF-20 alloy, with 477 precipitates. The precipitates in the René-88 DT alloy have a complex dendritic shape which is far more difficult to describe than the nearly cuboidal shapes found in the UMF-20 alloy.

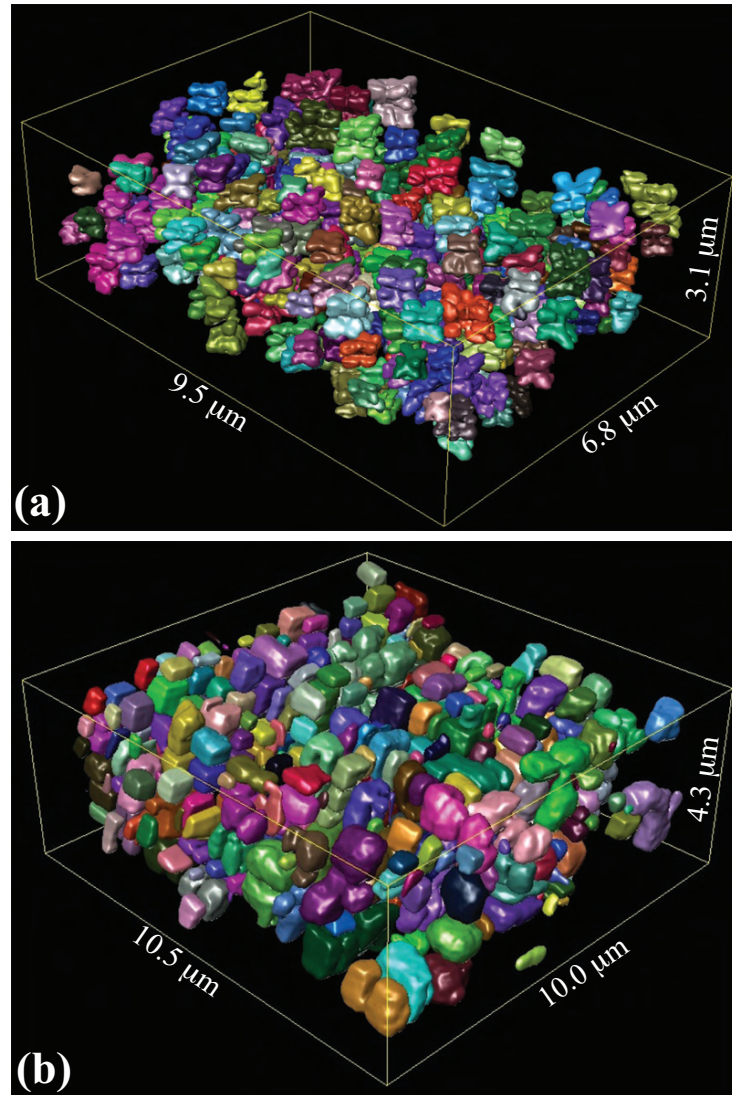


Figure I: Visualization of the 3-D microstructure of (a) René-88 DT and (b) UMF-20. The box dimensions are (a) $9.5 \times 6.8 \times 3.1 \mu\text{m}^3$ and (b) $10.5 \times 10.0 \times 4.3 \mu\text{m}^3$. There are 260 precipitates in (a), and 477 in (b); precipitate coloring is random so that individual precipitates can be distinguished.

The UMF-20 data set consists of 477 γ' precipitates completely contained within a volume of $10.5 \times 10.0 \times 4.3 \mu\text{m}^3$, with a mean precipitate volume of $0.1596 \mu\text{m}^3$. The aspect ratio scatter plot for this set of precipitates is shown in Fig. II(a), along with a contour plot of the aspect ratio distribution. Although there is a wide range of aspect ratios, the points tend to cluster near the oblate line ($\tau_1 = \tau_2$). While this plot is consistent with a qualitative examination of the 3-D visualization shown in Fig. I(b), it provides only limited morphological information.

Fig. II(b) shows the distribution of the γ' precipitates in the normalized moment invariant space. Note that the majority of points are clustered in the region $0.8 \leq \bar{\Omega}_3 \leq 1.0$, the former value being close to that of the cube. This indicates that the majority of precipitates have morphologies which range between those of the rectangular prisms ($\bar{\Omega}_3 = 0.7878$) and the ellipsoids ($\bar{\Omega}_3 = 1$). This “cuboidal” morphology can be observed clearly in the 3-D visualization in Fig. I(b). Since $\bar{\Omega}_1$ and $\bar{\Omega}_2$ can be thought of principally as aspect ratio descriptors, we note that the range of values observed for $\bar{\Omega}_1$ and $\bar{\Omega}_2$ is in agreement with the results seen in the aspect ratio scatter plot of Fig. II(a).

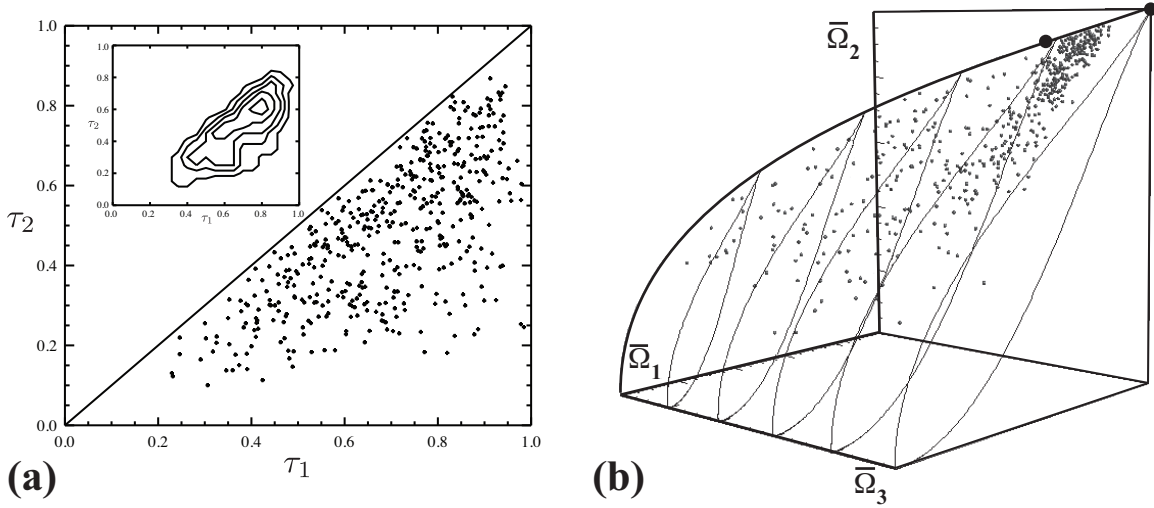


Figure II: (a) aspect ratio plot for the 477 γ' precipitates of the UMF-20 alloy; the inset shows the contour plot of the aspect ratio distribution. (b) shows the distribution of the precipitates in the normalized moment invariant space. The two solid circles on the isotropic curve represent the cube and the sphere.

Since $\bar{\Omega}_3$ is an affine invariant, a plot of $\bar{\Omega}_3$ as a function of precipitate volume can be used to determine if there is a systematic variation in precipitate morphology with precipitate size (Fig. III(a)). The dashed line indicates the value of $\bar{\Omega}_3$ for the class of rectangular prisms. We note that the points are principally located within the “cuboidal” region ($0.7878 \leq \bar{\Omega}_3 \leq 1$). Overall within this “cuboidal” region there is little change in morphology over a range of precipitate volumes.

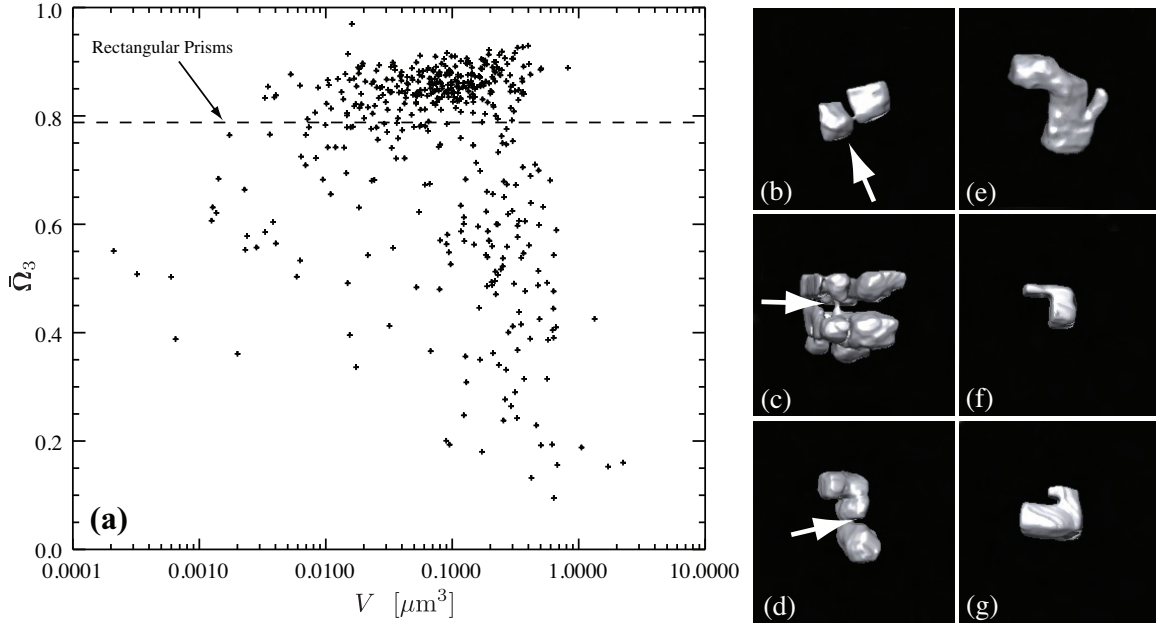


Figure III: (a) log-linear plot of $\bar{\Omega}_3$ vs. precipitate volume; most particles lie above the “prism” line. The majority of the particles below the line are morphological outliers, as shown in (b) through (g).

Most of the precipitates that lie below the “prism” line correspond to morphological outliers. There are two classes of outliers: artificial outliers, which result from segmentation errors (examples are shown in Fig. III(b)–(d); connecting ligatures, which are segmentation errors, are indicated by arrows), and naturally occurring outliers, often with L-shaped morphology, which are a product of the microstructural evolution (examples in Fig. III(e)–(g)). To evaluate the assumption that the points below the “prism” line in Fig. III(a) are indeed due to the morphological outliers, we introduce a new shape parameter, V/V_{conv} , the ratio of the particle volume to the volume of the convex hull of the particle. This provides a measure for the convexity of a given shape. Cuboidal precipitates are expected to have values of V/V_{conv} close to 1. This is illustrated in Fig. IV, where $\bar{\Omega}_3$ is plotted as a function of the shape quotient Q . The data points are colored according to the value of V/V_{conv} . Note that the precipitates within the “cuboidal” region are nearly convex, with values of V/V_{conv} near 1. To provide a reference point, the value of $\bar{\Omega}_3$ and Q for the regular rectangular prism is indicated on the plot by the grey square. The plot shows a strong correlation between the three parameters $\bar{\Omega}_3$, Q and V/V_{conv} . All points which lie outside the dense cloud of points can be considered as outliers, and a further analysis must be used to distinguish between the two classes of outliers; such an analysis may include the use of higher order moment invariants.

Fig. V(a) shows the results of a moment invariant analysis of 260 dendritic γ' precipitates in the René-88 DT alloy, represented in the normalized moment invariant space. Most precipitates

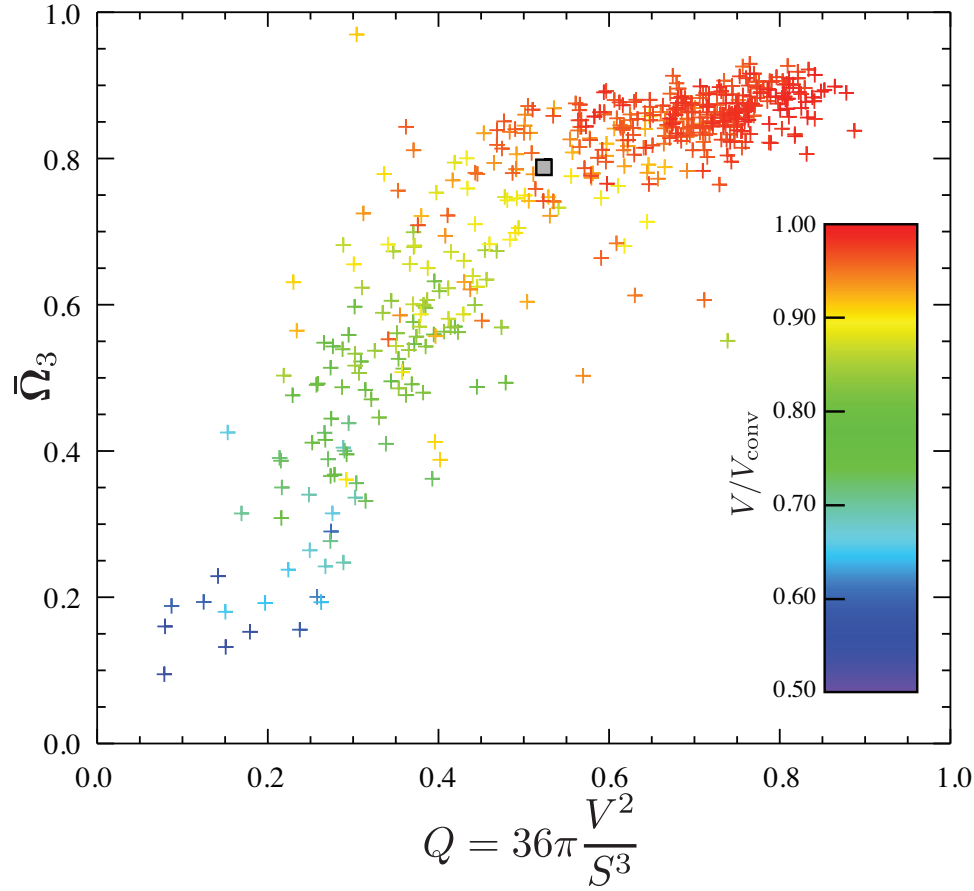


Figure IV: Plot of $\bar{\Omega}_3$ as a function of Q for 477 γ' precipitates from a UMF-20 nickel based superalloy. The points are colored according to the value of V/V_{conv} , which provides a measure of the precipitate convexity. High surface area particles lie on the lower left of the figure. The gray square indicates the location of the cube, whereas the upper right corner corresponds to the sphere.

are clustered close to the isotropic curve, in agreement with the 3-D visualization (Fig. 8(a) in Part I) which does not reveal any precipitates with a large aspect ratio. The wide range of $\bar{\Omega}_3$ values in Fig. V(a) indicates that a range of morphologies, very different from cuboidal or ellipsoidal, is present in the experimental data-set. The highly dendritic nature of the larger precipitates gives rise to a large surface-to-volume ratio, or, equivalently, a small value of the dimensionless shape quotient Q .

The relationship between $\bar{\Omega}_3$ and Q is illustrated Fig. V(b). The data points are colored according to the precipitate volume. Points corresponding to the precipitates in the inset are indicated with black circles. The variation of precipitate morphology with size is clearly visible from this plot. As the precipitates grow in size, they appear to follow a trajectory within the $\bar{\Omega}_3 - Q$ plot; they start out as near-cubes (near the point (0.524, 0.788) in the upper right hand

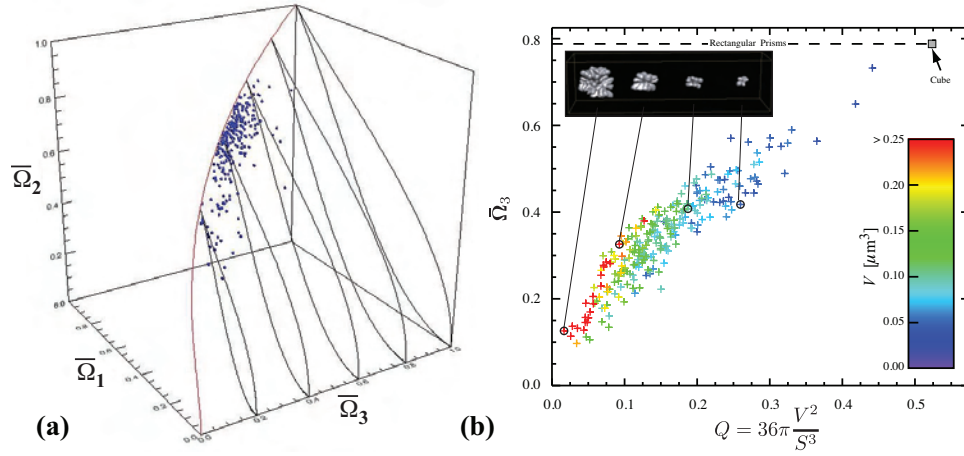


Figure V: (a) Plot of the calculated normalized second order moment invariants for 260 γ' precipitates. (b) Plot of \bar{Q}_3 as a function of Q for the 260 γ' precipitates from a René 88-DT superalloy. The color scheme corresponds to the particle volume. The precipitates shown in the inset correspond to the black circles. The horizontal dashed line provides indicates the location of the class of rectangular prisms, with the cube located at the position indicated on the far right.

corner) and, as they grow and evolve into a more complex dendritic shape, they “move” to the lower left corner of the diagram, corresponding to larger volume, larger surface area, and smaller affine moment invariant \bar{Q}_3 . A simpler characterization based solely on the particle size distribution and the aspect ratios would not be capable of revealing this correlation between the three parameters shown in Fig. V(b). Despite the complexity of the dendritic precipitate shapes, the combined use of the moment invariant \bar{Q}_3 and the shape quotient Q provides a quantitative description of the variation of precipitate morphology with precipitate size.

The results obtained in this research project show that it is possible to describe and quantify the shapes of secondary γ' precipitates in Ni-based superalloys in a quantitative way, by making use of the concept of moment invariants. This approach is quite general, easy to implement, and is not restricted to a particular class of shapes; indeed, our earlier theoretical paper on 3-D moment invariants [10] shows that the approach is valid for *all* 3-D shapes.

While it is not possible to reconstruct a 3-D shape when only its second order moments are known; an arbitrary shape can be reconstructed exactly only if *all* its moments are known. Therefore, the second order moment invariant approach is the lowest order approach possible (the first order moments do not contain any useful shape information other than the center-of-mass). Given how simple it is to compute the moment invariants, it is somewhat surprising that they have not been used before in the study of precipitate shapes. Particle aspect ratios have been used in the past to describe certain aspects of microstructures, but our theoretical work in this area clearly shows that there is an additional quantity that must be considered at the same level as the aspect

ratios of a shape; that is the affine invariant, $\bar{\Omega}_3$, which is a descriptor of shape classes. Therefore, if one desires to construct a description of a shape based on its aspect ratios, then one must also include the affine invariant, since it is also a second order parameter; indeed, it is the *only* other second order parameter that is invariant with respect to affine coordinate transformations. The correlations between $\bar{\Omega}_3$ and Q , shown in Figs. IV and V(b) show a different average slope for the two shape classes, indicating that the shape quotient provides additional shape information, not captured by the moment invariants.

From a numerical point of view, it is straightforward to compute higher-order moments μ_{pqr} ($p+q+r > 2$), and there is some literature on the invariants of third order. It is easy to show that the third order moments all vanish for a shape with inversion symmetry (most of the shapes considered in this study have approximate inversion symmetry, so that such a third-order analysis would not be very meaningful in this case). The number of invariants increases rapidly with increasing moment order, so that it becomes more difficult to represent them in a graphical way, similar to the normalized moment invariant space used in this paper. Despite these difficulties, there may be some benefit in considering the inclusion of third and fourth order moment invariants in the description of shapes. For statistical distributions, the moments correspond to the following quantities: variance (second order), skewness (third order), and kurtosis (fourth order). In addition, kurtosis and variance are often combined in the kurtosis excess. All of these parameters are important to the description of the shape of a statistical distribution, and we anticipate that they will also be important (in invariant form) for the description of actual 3-D shapes. In addition, there may be some benefit in combining the moment invariant approach with an analysis of the Minkowski functionals [11] of a given shape, using the dimensionless approach of the Blaschke diagram.

I.II Higher order moment invariants in 2-D and 3-D

We have expanded our study of moment invariants and employed a description of shapes based on 2-D and 3-D moments of second order. In 1-D, the second order moment of a distribution is generally known as its *variance* (i.e., a measure for the width of the distribution). The third and fourth order moments are known as *skewness* and *kurtosis*, respectively, and provide additional information about the shape of the distribution. In 2-D and 3-D, similar higher order moments can be defined. The number of moments increases rapidly with increasing order, and, in addition, they depend on the choice of reference frame, so that it becomes imperative to determine which combinations of moments are invariant with respect to affine and/or similarity transformations.

In 3D, the central geometric (cartesian) moments can be defined as

$$\mu_{pqr} = \iiint_{-\infty}^{+\infty} d\mathbf{r} x^p y^q z^r D(\mathbf{r}) = \iiint_D d\mathbf{r} x^p y^q z^r, \quad (1)$$

where $D(\mathbf{r})$ is the object's shape function. The derivation of moment invariant combinations is based on the existence of invariant geometric primitives.

There are four invariant geometric primitives in 3D: the distance between two points, the area of a triangle formed by three points, the dot product between two vectors connecting three points, and the volume of the irregular tetrahedron formed by four non-coplanar points. If we place one of these points in the origin, then the invariants can be written as (omitting constant pre-factors of 1/2 for A and 1/6 for V):

$$d(i) = |\mathbf{r}_i|; \quad (2a)$$

$$A(i, j) = |\mathbf{r}_i \times \mathbf{r}_j|; \quad (2b)$$

$$p(i, j) = \mathbf{r}_i \cdot \mathbf{r}_j; \quad (2c)$$

$$V(i, j, k) = (\mathbf{r}_i \times \mathbf{r}_j) \cdot \mathbf{r}_k. \quad (2d)$$

Rotational moment invariants can now be obtained by considering integrals of powers of products of these invariant primitives over the volume of the object:

$$J_{dApV}^{\alpha\beta\gamma\delta}(i, j, \dots, p) = \iiint_{-\infty}^{+\infty} d\mathbf{r}_i d\mathbf{r}_j \dots d\mathbf{r}_p d(i)^\alpha A(j, k)^\beta p(l, m)^\gamma V(n, o, p)^\delta D(\mathbf{r}_i) D(\mathbf{r}_j) \dots D(\mathbf{r}_p). \quad (3)$$

By substituting the coordinate expressions for the primitives into this integral and rewriting the integrals as products of geometric moments, one obtains many expressions for potential invariants. Note that the notation $p(l, m)^\gamma$ includes both $p(1, 2)^2$ and $p(1, 2)p(1, 3)$; i.e., multiple sets of points can (and should) be used to enumerate all invariants.

Our derivations show that this approach does indeed reproduce all three moment invariants of second order:

$$\begin{aligned} J_{dApV}^{2000}(1) &= \iiint_{-\infty}^{+\infty} d\mathbf{r}_1 d(1)^2 D(\mathbf{r}_1) \\ &\rightarrow J_1 = (\mu_{200} + \mu_{020} + \mu_{002}) / \mu_{000}^{5/3}. \end{aligned}$$

$$\begin{aligned} J_{dApV}^{0200}(1, 2) &= \iiint_{-\infty}^{+\infty} d\mathbf{r}_1 d\mathbf{r}_2 A(1, 2)^2 D(\mathbf{r}_1) D(\mathbf{r}_2) \\ &\rightarrow J_2 = (\mu_{200}\mu_{020} + \mu_{020}\mu_{002} + \mu_{002}\mu_{200} - (\mu_{110}^2 + \mu_{101}^2 + \mu_{011}^2)) / \mu_{000}^{10/3}. \end{aligned}$$

$$\begin{aligned} J_{dApV}^{0002}(1, 2, 3) &= \iiint_{-\infty}^{+\infty} d\mathbf{r}_1 d\mathbf{r}_2 d\mathbf{r}_3 V(1, 2, 3)^2 D(\mathbf{r}_1) D(\mathbf{r}_2) D(\mathbf{r}_3) \\ &\rightarrow J_3 = (\mu_{200}\mu_{020}\mu_{002} + 2\mu_{110}\mu_{101}\mu_{011} - \mu_{200}\mu_{011}^2 - \mu_{020}\mu_{101}^2 - \mu_{002}\mu_{011}^2) / \mu_{000}^5. \end{aligned}$$

We have completed the derivation of all possible third order invariants (we have found 13 of them). The explicit expressions for the invariants are lengthy and not particularly illuminating, so here we only report the integrands that give rise to the invariants shown in Table 3.

Integrand	Invariant	Order	Exponent
$d(1)^3$	(series)	3	2 (3)
$p(1, 2)^3$	K_1	3	4 (3, 3)
$d(1)^2 d(2)^2 p(1, 2)$	K_2	3	4 (3, 3)
$p(1, 2) A(1, 2)^2$	$\frac{1}{2}(K_2 - K_1)$	3	4 (3, 3)
$V(1, 2, 3)^3$	0	3	6 (3, 3, 3)
$V(1, 2, 3) d(1)^2 d(2)^2 d(3)^2$	0	3	6 (3, 3, 3)
$V(1, 2, 3) A(1, 2)^2 d(3)^2$	0	3	6 (3, 3, 3)
$V(1, 2, 3) p(1, 2)^2 d(3)^2$	0	3	6 (3, 3, 3)
$p(1, 2) p(1, 3) p(1, 4) d(2)^2 d(3)^2 d(4)^2$	K_9	3	8 (3, 3, 3, 3)
$V(1, 2, 3) V(1, 2, 4) V(1, 3, 4) V(2, 3, 4)$	K_{12}	3	8 (3, 3, 3, 3)
$p(1, 2) p(3, 4) d(1)^2 d(2)^2 d(3)^2 d(4)^2$	K_2^2	3	8 (3, 3, 3, 3)
$p(1, 4) p(2, 3) d(2)^2 d(4)^2 A(2, 3)^2$	$K_2(K_2 - K_1)$	3	8 (3, 3, 3, 3)
$d(1) A(1, 2)^2$	(series)	3	11/3 (3, 2)
$V(1, 2, 3) p(2, 3) d(1)^2$	0	3	16/3 (3, 2, 2)
$V(1, 2, 3) p(1, 2) p(3, 4) d(4)^2$	0	3	21/3 (3, 2, 2, 2)
$p(1, 2) p(2, 3)^2 d(1)^2$	K_3	3	17/3 (3, 3, 2)
$p(1, 2) p(2, 3) d(1)^2 d(3)^2$	K_4	3	17/3 (3, 3, 2)
$p(1, 2) A(2, 3)^2 d(1)^2$	K_8	3	17/3 (3, 3, 2)
$V(1, 2, 3)^2 p(1, 2)$	K_{13}	3	17/3 (3, 3, 2)
$p(1, 2) p(2, 3) p(3, 4) d(1)^2 d(4)^2$	K_5	3	22/3 (3, 3, 2, 2)
$p(1, 2) p(2, 3) p(3, 4) A(1, 4)^2$	K_6	3	22/3 (3, 3, 2, 2)
$p(1, 3) A(1, 2)^2 A(3, 4)^2$	K_7	3	22/3 (3, 3, 2, 2)
$V(1, 2, 3) V(1, 2, 4) A(3, 4)^2$	K_{10}	3	22/3 (3, 3, 2, 2)
$V(1, 2, 3) V(1, 2, 4) p(3, 4)^2$	K_{11}	3	22/3 (3, 3, 2, 2)
$V(1, 2, 3) V(1, 2, 4) V(2, 3, 4) p(1, 3)$	0	3	23/3 (3, 3, 3, 2)
$V(1, 2, 3) A(1, 2)^2 p(3, 4) d(4)^2$	0	3	23/3 (3, 3, 3, 2)

Table 3: All possible combinations for the integrand that result in third order moment invariants. Explicit expressions for the parameter K_i are available upon request.

In 2D, the derivation of higher order moment invariants is simplified by starting from complex moments, defined as:

$$c_{pq} = \iint D(x, y)(x + iy)^p(x - iy)^q dx dy = \int_0^\infty \int_0^{2\pi} d\theta dr r^{p+q+1} e^{i(p-q)\theta} D(r, \theta), \quad (4)$$

where the second integral employs polar coordinates. Flusser, Suk, and Zitová [12] have shown that rotational invariants, I , of order n can be constructed as

$$I = \prod_{i=1}^n c_{p_i q_i}^{k_i} \quad \text{with} \quad \sum_{i=1}^n k_i(p_i - q_i) = 0. \quad (5)$$

Using their approach, we have shown that there are six rotational moment invariants of third order, four of them are similarity invariants, and two are skew invariants. They are given by:

$$c_{11}, c_{21}c_{12}, \Re[c_{20}c_{12}^2], \Re[c_{30}c_{12}^3]; \quad \Im[c_{20}c_{12}^2], \Im[c_{30}c_{12}^3]. \quad (6)$$

In addition, there are affine invariants of order r , which are derived from the following integrals (in a manner similar to that used for the 3-D affine invariants):

$$I(D) = \iiint \cdots \iiint \prod_{k,j=1}^r C_{kj}^{n_{kj}} \prod_{i=1}^r D(x_i, y_i) dx_i dy_i \quad (7)$$

with

$$C_{ij} = x_i y_j - x_j y_i. \quad (8)$$

Flusser and Suk have shown that there are 80 independent affine invariants of order less than or equal to 12. We have created an efficient and accurate algorithm to compute all affine, similarity, and skew 2-D moment invariants of a binary object of order up to and including 12. This algorithm has been used in the final year of this project to analyze the shapes of γ' precipitates in 2-D sections (electron or optical micrographs) of a variety of Ni-based superalloys. Several OEMs (GEAE, Rolls Royce) have expressed an interest in the use of shape moments and moment invariants to study precipitate shapes from 2D sections instead of in 3D; we have started the analysis of the relation between 2D and 3D moment descriptions, and we expect to be able to submit a paper on this topic to Acta Materialia in early 2011.

I.III Shape fitting using Zernike moments

In addition to cartesian moments, one can also use other moments to describe shapes. One particular class of moments of interest for our work is known as the *Zernike moments*. These moments are defined with respect to the Zernike functions, which are essentially spherical harmonics modulated by radial functions in such a way that the set of functions is orthonormal inside the unit ball.

Mathematically, the Zernike functions are defined as (using spherical coordinates (r, θ, ϕ)) [13]:

$$Z_{nl}^m(\mathbf{r}) = \sum_{\nu=0}^k q_{kl}^{\nu} r^{2\nu+l} Y_l^m(\theta, \phi), \quad (9)$$

where $k = (n - l)/2$ and

$$q_{kl}^{\nu} = \frac{(-1)^{k+\nu}}{2^{2k}} \sqrt{2l+4k+3} \binom{2k}{k} \binom{k}{\nu} \binom{2(k+l+\nu)+1}{2k} \binom{k+l+\nu}{k}^{-1}. \quad (10)$$

The Zernike moments for an object are then defined as follows:

$$\Omega_{nl}^m = \iiint d\mathbf{r} D(\mathbf{r}) Z_{nl}^m(\mathbf{r}), \quad (11)$$

where $D(\mathbf{r})$ is the shape function of the object. Since the functions are only defined inside the unit ball, the object must be scaled to fit inside the ball, typically with a maximal radius of 0.75. The Zernike moments can be computed explicitly in term of the cartesian moments μ_{pqr} :

$$\Omega_{nl}^m = c_l^m \sum_{\nu=0}^{\frac{n-l}{2}} q_{nl}^{\nu} \sum_{\mu=0}^{\lfloor \frac{l-m}{2} \rfloor} \frac{(-1)^{m+\mu}}{2^{m+2\mu}} \binom{l}{\mu} \binom{l-\mu}{m+\mu} \sum_{\alpha=0}^m (-i)^{m-\alpha} \binom{m}{\alpha} \sum_{\kappa=0}^{\nu} \binom{\nu}{\kappa} \sum_{\beta=0}^{\kappa+\mu} \binom{\kappa+\mu}{\beta} \times$$

$$\mu_{2\beta+\alpha, 2(\kappa+\mu-\beta)+m-\alpha, 2(\nu-\kappa-\mu)+l-m}.$$

The rotationally invariant moments F_{nl} are computed by taking the norm over all values of m . For the cube with edge length L , the resulting low order rotationally invariant Zernike moments are (all invariants with odd n vanish):

$$\begin{aligned} F_{00} &= 4L^3 \sqrt{\frac{3}{\pi}}; \\ F_{20} &= 2L^3 \sqrt{\frac{7}{\pi}} |3 - 5L^2|; \\ F_{40} &= \frac{1}{10} L^3 \sqrt{\frac{11}{\pi}} |75 - 350L^2 + 399L^4|; \\ F_{44} &= \frac{4}{5} L^7 \sqrt{\frac{231}{\pi}}; \\ F_{60} &= \frac{1}{28\sqrt{15\pi}} L^3 |3675 - 33075L^2 + 92169L^4 - 83369L^6|; \end{aligned}$$

$$\begin{aligned} F_{64} &= 2L^7 \sqrt{\frac{1}{35\pi}} |231 - 481L^2|; \\ F_{66} &= \frac{16}{7} L^9 \sqrt{\frac{130}{3\pi}}; \\ F_{80} &= \frac{1}{3360} L^3 \sqrt{\frac{19}{\pi}} |33075 - 485100L^2 + 2396394L^4 - 5002140L^6 + 3823963L^8|. \end{aligned}$$

We have created a series of algorithms for the efficient numerical computation of the Zernike functions and moments. An example comparison between numerical and theoretical values for a cube are shown in Table 4.

Ω_n	Theory	Numerical	% diff.
F_{00}	0.094410	0.094410	0.0
F_{20}	0.186197	0.186197	0.0
F_{40}	0.219383	0.219383	0.0
F_{44}	0.001156	0.001157	0.0
F_{60}	0.189271	0.189271	0.0
F_{64}	0.006137	0.006137	0.0
F_{66}	0.000120	0.000120	0.0
F_{80}	0.115630	0.115629	0.0

Table 4: Theoretical and computed rotationally invariant Zernike moments along with the relative errors for a cube with edge length $L = 0.289063$ ($= 18.5/64.0$).

The reconstruction of a shape function $D(\mathbf{r})$ from its moments is performed by the following general summation:

$$D(\mathbf{r}) = \sum_{n=0}^{\infty} \sum_{l=0}^n \sum_{m=-l}^l \Omega_{nl}^m Z_{nl}^m(\mathbf{r})$$

where only terms with $n - l$ even are taken into account. We have used this approach to fit the shapes of γ' precipitates in UMF-20 and Rene-88 DT superalloys.

Fig. VI shows shape fits for two γ' particles; in (a)-(b), a UMF-20 cuboidal particle is shown along with its fit using Zernike moments up to order $n = 20$. The agreement between the experimental shape and the reconstructed shape is quite good, indicating that the Zernike moment approach may become useful for the description of precipitates with relatively simple shapes. In Fig. VI(c)-(d), a fit of a dendritic γ' particle from a Rene-88 DT alloy is shown. Again, 20 orders of Zernike moments were used. While the reconstructed shape does resemble the experimental shape, it is clear that additional moments are needed to fully reproduce the correct shape.

We plan to use this approach to generate particles within a desired shape class. For instance, one could compute the Zernike moments for a large number of experimental precipitates, and then use the distributions of moments to sample new moments and create similar shapes. Such an approach might become useful for the creation of digital microstructures.

I.IV Application to synthetic microstructures

The observations described in the previous section have an impact in the area of digitally synthesized microstructures, in particular the quantitative comparison of experimental and simulated

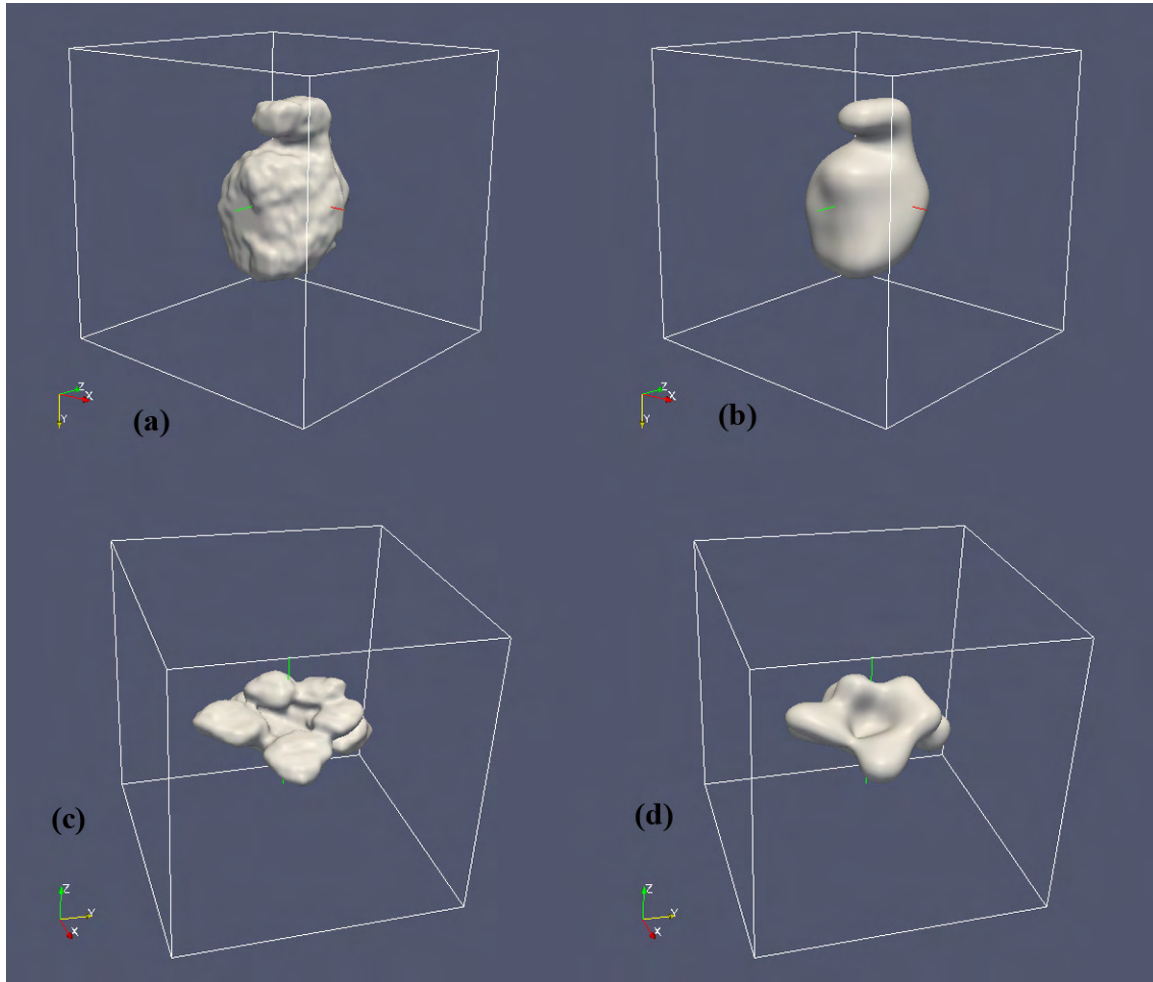


Figure VI: Experimental ((a) and (c)) and reconstructed ((b) and (d)) shapes of γ' precipitates in UMF-20 (top row) and Rene-88 DT (bottom row) alloys, using 20 orders of Zernike moments.

microstructures. The moment invariant approach removes the subjective comparison of 3-D visualizations of experimental and modeled microstructures and replaces it with an objective and quantitative comparison. If a numerical model of a microstructure is to be a correct representation of a real microstructure, then, at the very least, the distribution of the microstructural components in the normalized moment invariant space should be the same for both microstructures. In other words, if a set of γ' precipitates, determined from an experimental 3-D reconstruction, occupies a certain region in the moment invariant space, then the precipitate shapes obtained from, for instance, a phase field simulation of this microstructure, should occupy the same region of the moment invariant space. If the two sets of points do not overlap, then the simulation parameters may need to be fine-tuned. Therefore, a moment invariant analysis can become an important tool to match simulation parameters to experimental microstructures.

We have worked with Dr. M. Groeber (AFRL) on the quantitative comparison of synthetic experimental microstructures. The programs used to generate microstructures are described in [14,15]; different starting shapes were used to create the final grain shapes: ellipsoids, superellipsoids, and cuboctahedra (the latter because they already have 14 facets, close to the average number of grain nearest neighbors in a real microstructure). Superellipsoids are defined in cartesian coordinates as:

$$\left|\frac{x}{a}\right|^n + \left|\frac{y}{b}\right|^n + \left|\frac{z}{c}\right|^n = 1. \quad (12)$$

where n is a positive real number. The equation describes a range of shapes, including cubes ($n = \infty$), cuboids ($n > 2$), octahedra ($n = 1$), ellipsoids ($n = 2$), and their anisotropically scaled equivalents. After the grains for the microstructure are generated, they are placed one at a time in the volume. After each grain is placed, the number and size of neighbors in the synthetic dataset is checked against the distribution from the experimental dataset. If placement does not match the experimental distribution, the grain is replaced and checked again. This is repeated until all grains have been placed, then Voronoi tessellation is used to fill space in the volume. Finally, crystallographic orientations are assigned to the grains to match the orientation distribution function, the misorientation distribution function, and the microtexture function. The various orientation distribution functions and microtexture function are not pertinent to shape characterization, so the accuracy with which they are assigned was not considered in our research.

Statistic	Experimental	Ellipsoidal	Superellipsoidal	Cuboctahedral
Min	1.04	1.11	1.16	1.05
Max	989.91	883.59	888.41	586.72
Median	17.67	19.50	36.69	24.55
Mean	46.29	41.51	53.13	38.23
Std Dev	75.59	69.13	59.69	43.48

Table 5: The minimum, maximum, median, mean, and standard deviation of volume in μm^3 for the experimental, ellipsoidal, superellipsoidal, and cuboctahedral datasets.

We begin by looking at basic descriptors of the microstructures, such as the grain size. The statistics for the grain size distributions of the four datasets are given in Table 5. The histograms for grain size are shown in Fig. VII. We can see that the minimum grain size of the three synthetic microstructures does not differ greatly from that of the experimental microstructure. The largest grains in the computer generated, synthetic microstructures tend to be smaller than the largest grains in the experimental microstructure. More importantly, we should examine the morphology of the largest grains.

The largest grains from each dataset are shown in Fig. VIII. The morphology of the experimental grain is quite different from that of the synthetic microstructures. It is long and has three relatively distinct sections which could either be representative of the true microstructure or due

to segmentation errors which could cause separate grains to join incorrectly. The ellipsoidal grain is essentially ellipsoidal with some surface roughness or concavity from when surrounding grains took volume from it.

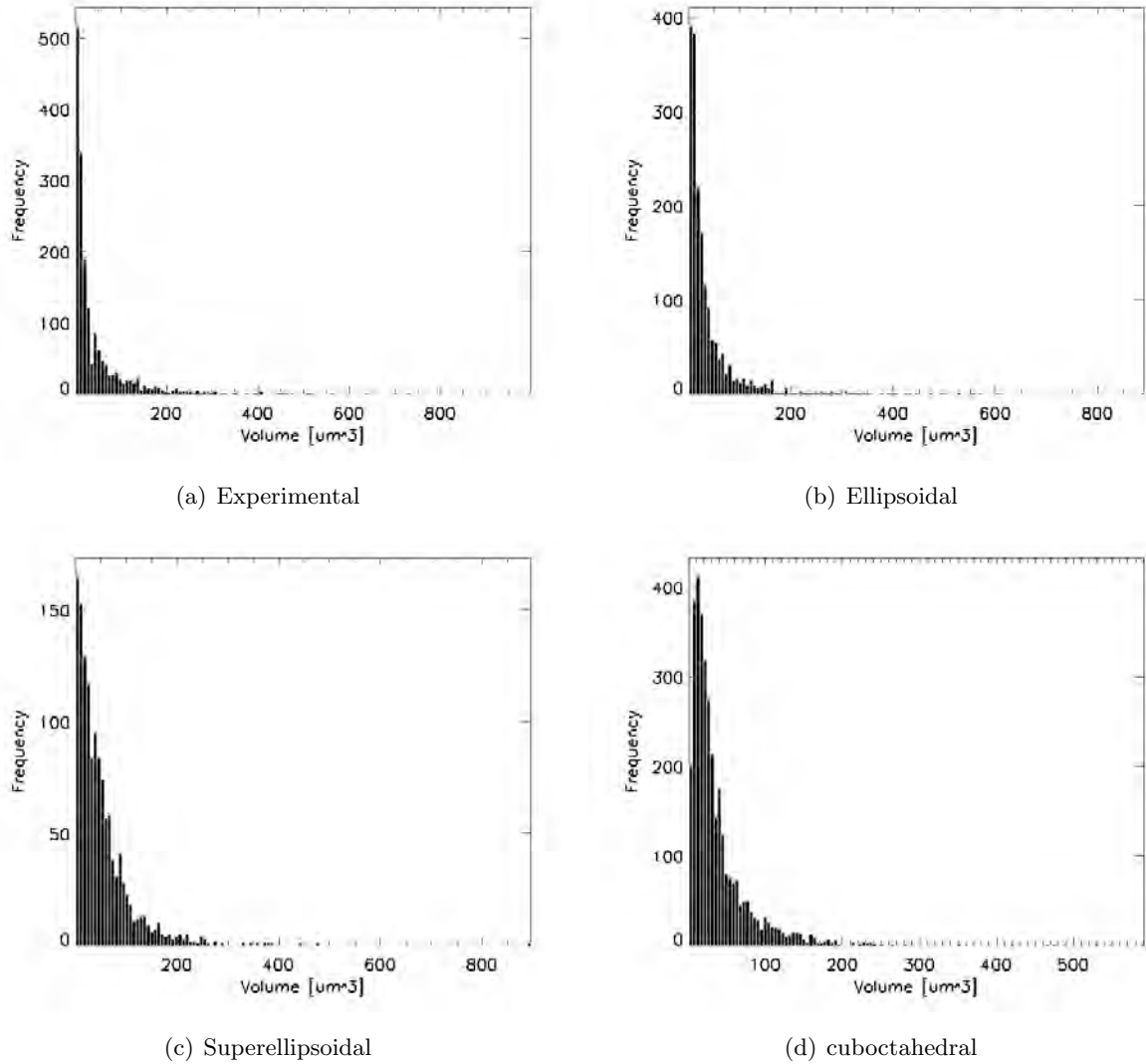


Figure VII: The volume histograms for the (a) experimental, (b) ellipsoidal, (c) superellipsoidal, and (d) cuboctahedral datasets.

The superellipsoidal and cuboctahedral grains look more like a grain from a real microstructure and not just simply like an ellipsoid. However, they do not have a similar morphology to the largest experimental grain as they do not have an appearance of multiple sections. Grains based on single instantiations of ellipsoidal, superellipsoidal, and cuboctahedral shapes do not approach the shape of the experimental grain because of its complexity. Two or more instantiations of different shape

classes would need to be joined in order to better match the complexity of the outlier experimental grains with multiple sections.

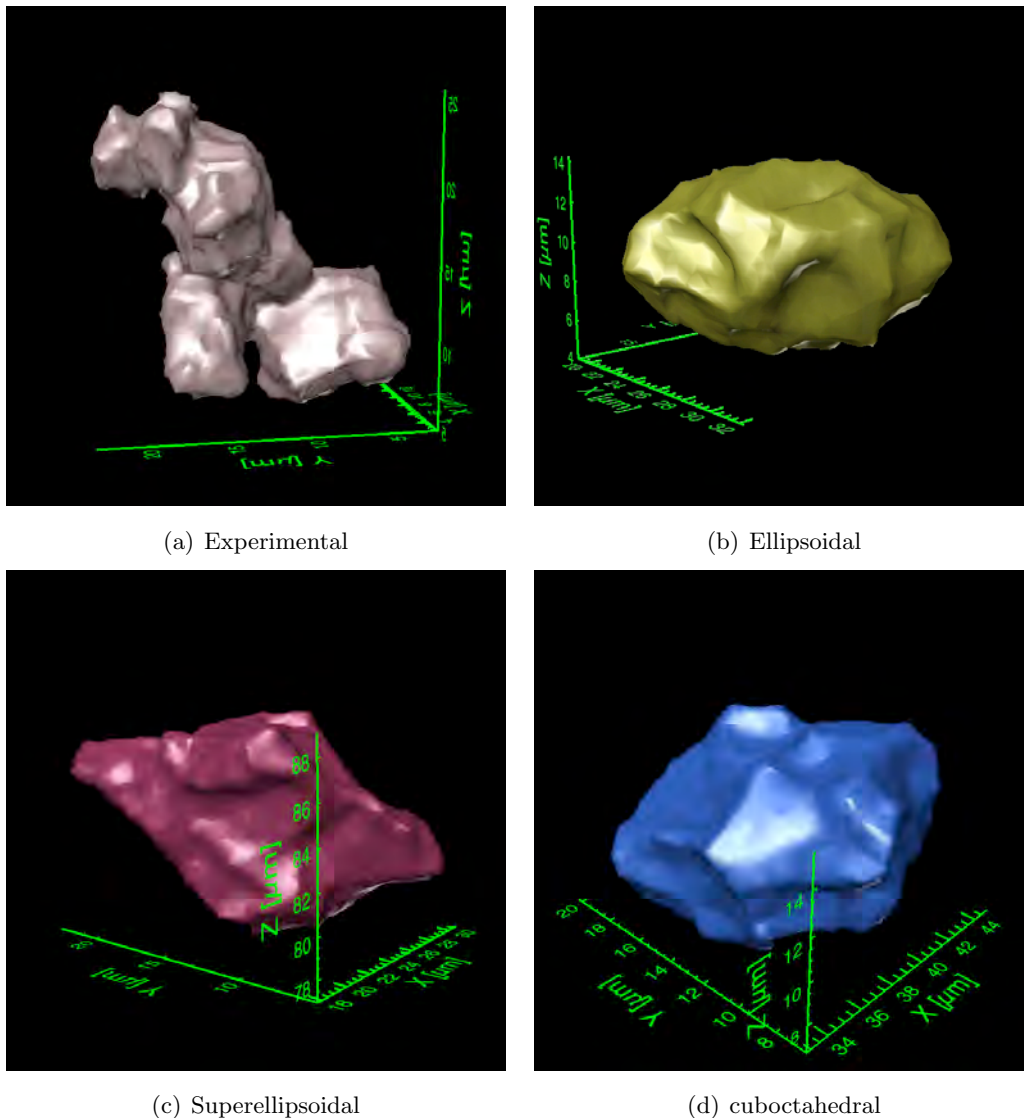


Figure VIII: Visualizations of the largest grains from the (a) experimental, (b) ellipsoidal, (c) superellipsoidal, and (d) cuboctahedral datasets.

We can see that the volume statistics of the experimental microstructure are actually matched best by the ellipsoidal microstructure, while the superellipsoidal microstructure does the worst job. This is particularly apparent when one looks at the mean and median values. The superellipsoidal dataset does a particularly bad job of matching the median value for the volume of the experimental microstructure.

The plots of aspect ratio τ_1 versus τ_2 are shown in Fig. IX. The basic statistics of τ_1/τ_2 are

Statistic	Experimental	Ellipsoidal	Superellipsoidal	Cuboctahedral
Min	1.00	1.00	1.01	1.00
Max	5.00	4.21	3.37	4.53
Median	1.34	1.42	1.37	1.35
Mean	1.39	1.57	1.44	1.42
Std Dev	0.279	0.485	0.322	0.315

Table 6: The minimum, maximum, median, mean, and standard deviation of the aspect ratio τ_1/τ_2 for the experimental, ellipsoidal, superellipsoidal, and cuboctahedral datasets.

given in Table 6. The mean, median, and standard deviations of τ_1/τ_2 for the experimental dataset are lower than those of the synthetic datasets, while the maximum τ_1/τ_2 value is highest for the experimental dataset. So, while on average the real grains tend to have an aspect ratio slightly smaller than the synthetic grains, the extreme values are higher for the experimental dataset. The cuboctahedral dataset matches the real dataset best of the synthetic datasets statistically. The histograms of τ_1/τ_2 are shown in Fig. X. The standard deviation of τ_1/τ_2 for the experimental microstructure is less than that of the synthetic microstructures, which we can also see as manifested in the smaller tail on the right side of the histogram for the experimental microstructure. With the experimental microstructure we tend to see fewer grains with aspect ratio larger than approximately two, while the synthetic microstructures tend to have more grains with aspect ratio greater than two.

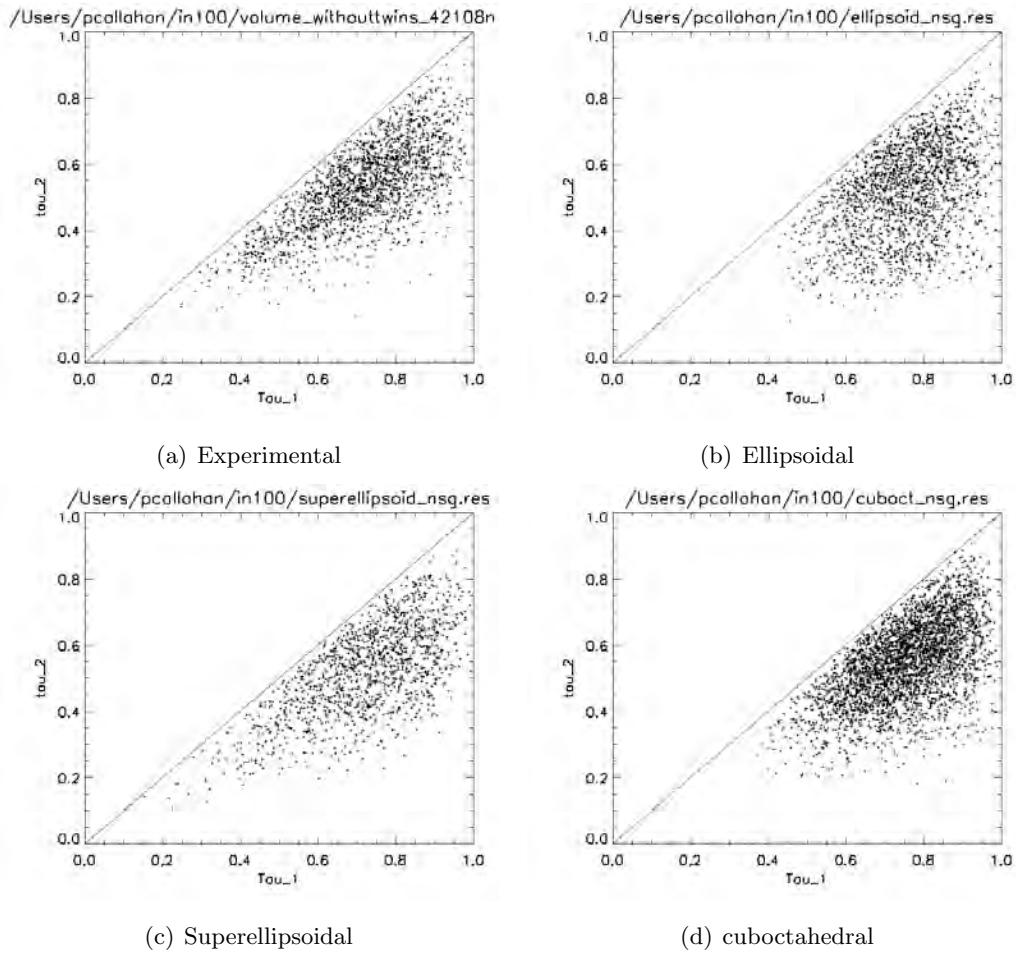
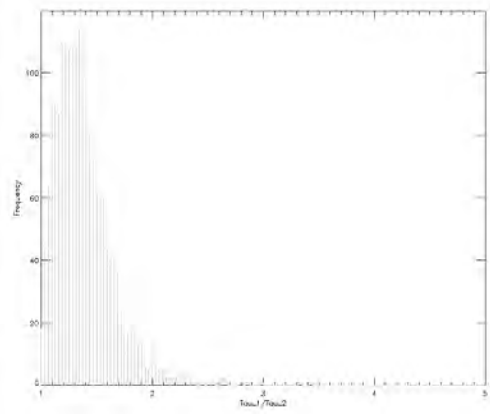
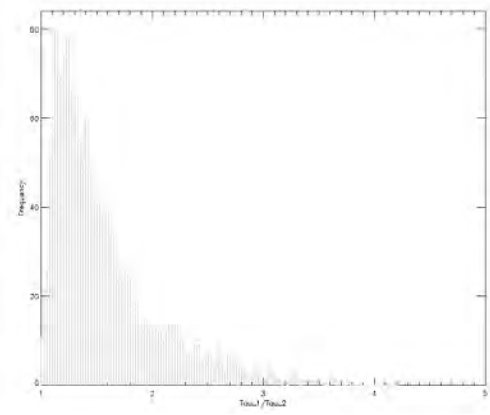


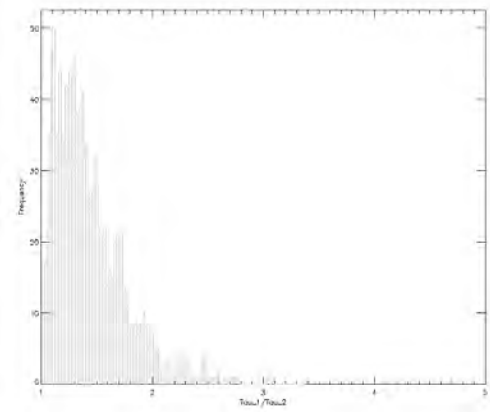
Figure IX: The aspect ratio plots for the (a) experimental, (b) ellipsoidal, (c) superellipsoidal, and (d) cuboctahedral datasets.



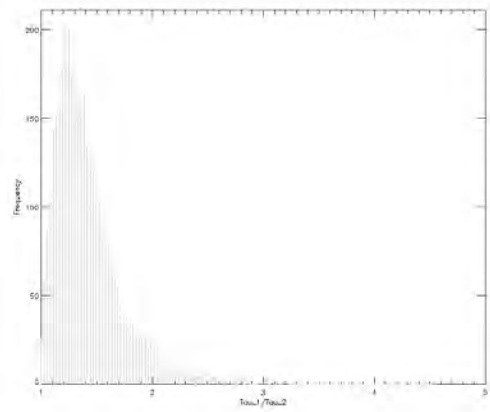
(a) Experimental



(b) Ellipsoidal



(c) Superellipsoidal



(d) cuboctahedral

Figure X: The histograms of τ_1/τ_2 for the (a) experimental, (b) ellipsoidal, (c) superellipsoidal, and (d) cuboctahedral datasets.

The grains with maximum aspect ratio are shown in Fig. XI. The volume and $\bar{\Omega}_3$ for the grains with maximum aspect ratio are given in Table 7.

Statistic	Experimental	Ellipsoidal	Superellipsoidal	Cuboctahedral
Volume (μm^3)	3.5	285.7	50.9	8.9
$\bar{\Omega}_3$	0.12	0.54	0.86	0.57

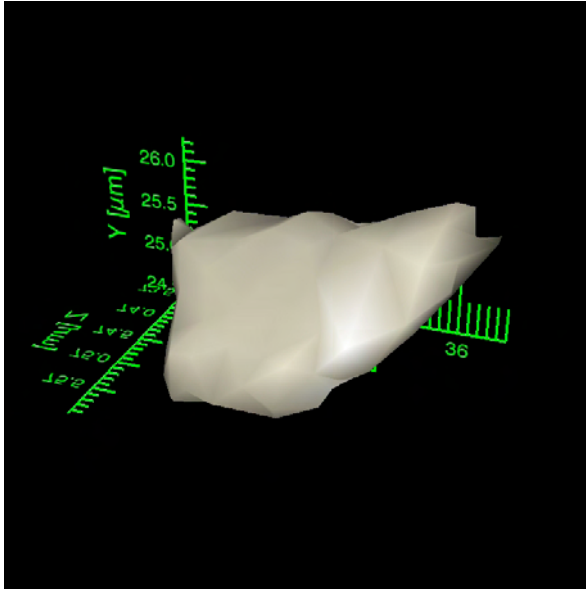
Table 7: The volume and $\bar{\Omega}_3$ of the grain with maximum aspect ratio τ_1/τ_2 for the experimental, ellipsoidal, superellipsoidal, and cuboctahedral datasets.

Statistic	Experimental	Ellipsoidal	Superellipsoidal	Cuboctahedral
Min	0.024	0.186	0.105	0.172
Max	0.877	0.950	0.871	0.893
Median	0.632	0.742	0.606	0.679
Mean	0.605	0.726	0.585	0.663
Std Dev	0.150	0.121	0.134	0.103

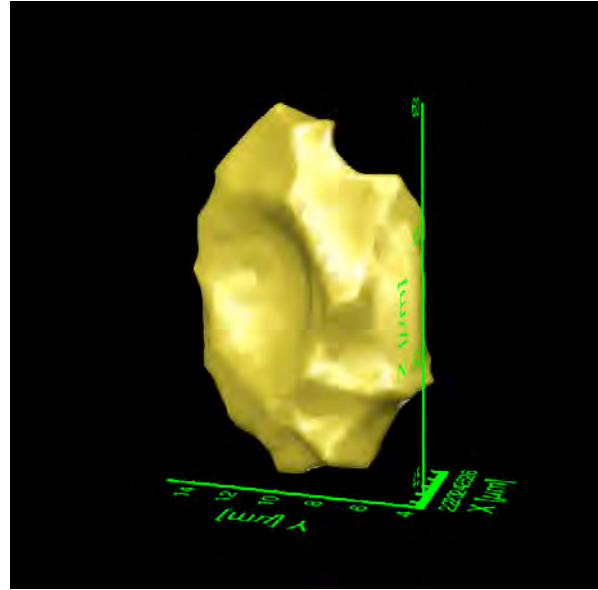
Table 8: The minimum, maximum, median, mean, and standard deviation of the second order moment invariant $\bar{\Omega}_3$ for the experimental, ellipsoidal, superellipsoidal, and cuboctahedral datasets.

The grains from each dataset plotted in moment invariant space are shown in Fig. XII. $\bar{\Omega}_3$ values for the grains with maximum aspect ratio τ_1/τ_2 for each dataset are given in Table 7. $\bar{\Omega}_3$ for the maximum aspect ratio grain of the experimental dataset is quite low, in fact it is lower than the minimum $\bar{\Omega}_3$ for the ellipsoidal and cuboctahedral datasets, and just above the minimum for the superellipsoidal dataset. The $\bar{\Omega}_3$ values for the maximum aspect ratio grain of the experimental, ellipsoidal and cuboctahedral datasets are all lower than their respective mean and median $\bar{\Omega}_3$. The $\bar{\Omega}_3$ values of the maximum aspect ratio grain for the superellipsoidal dataset is larger than its mean and median, and is actually very near the maximum value of $\bar{\Omega}_3$. In the experimental dataset, high aspect ratio grains tend to have much more complex morphologies compared with their average grains. In the ellipsoidal and cuboctahedral datasets, the high aspect ratio grains tend to be more complex, but their morphologies are not as complex as their experimental counterparts. It is interesting that in the superellipsoidal dataset, the highest aspect ratio grain does not have a particularly complex morphology as measured by moment invariants.

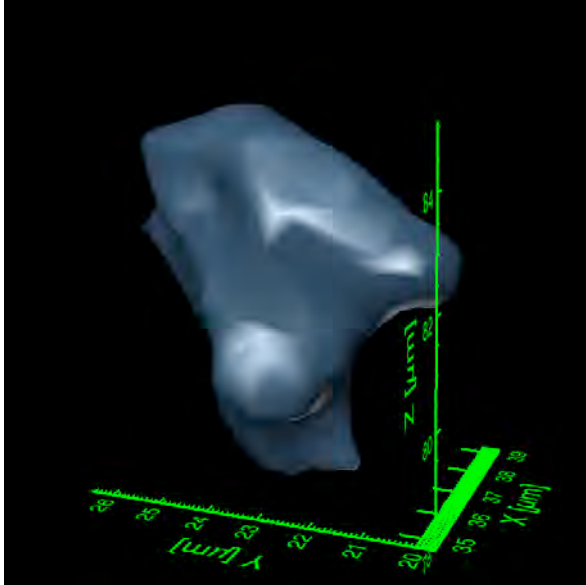
The basic statistics for $\bar{\Omega}_3$ for each of the datasets are given in Table 8. The ellipsoidal and cuboctahedral datasets have larger means and medians than the experimental dataset, while the superellipsoidal dataset has a smaller mean and median than the experimental dataset. This indicates that the experimental dataset is more complex than ellipsoidal and cuboctahedral datasets, and slightly less complex than the superellipsoidal dataset. Also, the minimum $\bar{\Omega}_3$ of the experimental dataset is much lower than any of the synthetic datasets. The maximum $\bar{\Omega}_3$ for the experimental,



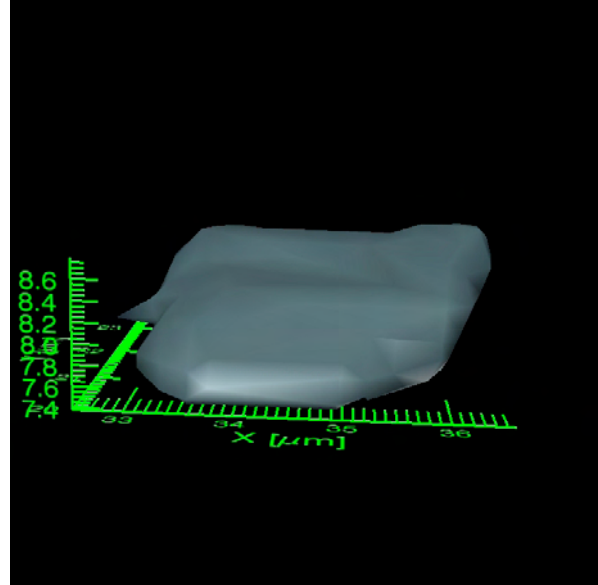
(a) Experimental



(b) Ellipsoidal



(c) Superellipsoidal



(d) cuboctahedral

Figure XI: The grains with maximum aspect ratio from the (a) experimental, (b) ellipsoidal, (c) superellipsoidal, and (d) cuboctahedral datasets.

superellipsoidal, and cuboctahedral datasets are all similar and less than 0.9, while the ellipsoidal dataset has a maximum of 0.95, which is near 1, the value of $\bar{\Omega}_3$ for an ellipsoidal shape. This is not surprising considering the starting grain shape would have been an ellipsoid in this dataset, and thus have $\bar{\Omega}_3 = 1$ before placement in the experimental volume when some volume can be taken from it by surrounding grains and any alteration of the shape due to the tessellation step during microstructure generation.

The plots of the datasets in normalized moment invariant space are given in Fig. XII. With all three datasets, the majority of the grains sit above approximately $\bar{\Omega}_3 = 0.5$, though we can see that the ellipsoidal dataset sits further to the right along the $\bar{\Omega}_3$ axis. It also appears that the grains in each dataset tend to sit near the isotropic curve, but particularly in the experimental and superellipsoidal datasets. The tail of grains that run near the isotropic curve towards lower values of $\bar{\Omega}_3$ is more pronounced in the experimental dataset than in the others. There is a noticeable lack of datapoints in the tail with low $\bar{\Omega}_3$ in the ellipsoidal and cuboctahedral dataset. The superellipsoidal dataset does have a tail with low values of $\bar{\Omega}_3$, however, they are further away from the isotropic curve than in the experimental dataset. This indicates that the grains with small $\bar{\Omega}_3$, those with more complex morphologies, in the superellipsoidal dataset tend to have higher aspect ratios than those in the experimental dataset, indicating that the cause of complex morphology in the experimental dataset is not being mimicked in the synthetic datasets. The superellipsoidal microstructure does a good job of matching the experimental microstructure in moment invariant space.

The basic statistics of the shape quotient Q are given in Table 9. Since Q is a ratio of surface area and volume which can be used as a measure of shape complexity. It has a maximum value of 1 for a sphere as a sphere has minimum surface area to volume, and decreases as surface area relative to volume increases, so decreasing Q corresponds to increasing complexity as measured by the surface area to volume ratio. We can see that the minimum, maximum, median, and mean of the cuboctahedral dataset match those of the experimental dataset well. Next best is the ellipsoidal dataset, followed by the superellipsoidal dataset, which does not match particularly well. The ellipsoidal dataset tends to have larger values of Q and so has less surface area relative to volume

Statistic	Experimental	Ellipsoidal	Superellipsoidal	Cuboctahedral
Min	0.201	0.200	0.198	0.306
Max	0.901	0.922	0.886	0.904
Median	0.719	0.760	0.623	0.711
Mean	0.684	0.729	0.611	0.699
Std Dev	0.128	0.119	0.130	0.096

Table 9: The minimum, maximum, median, mean, and standard deviation of the shape quotient Q for the experimental, ellipsoidal, superellipsoidal, and cuboctahedral datasets.

than the experimental dataset. The superellipsoidal dataset tends to have smaller values of Q and so has more surface area to volume relative to the experimental dataset. So it is apparent that the surface area to volume does change depending on the starting grain shape.

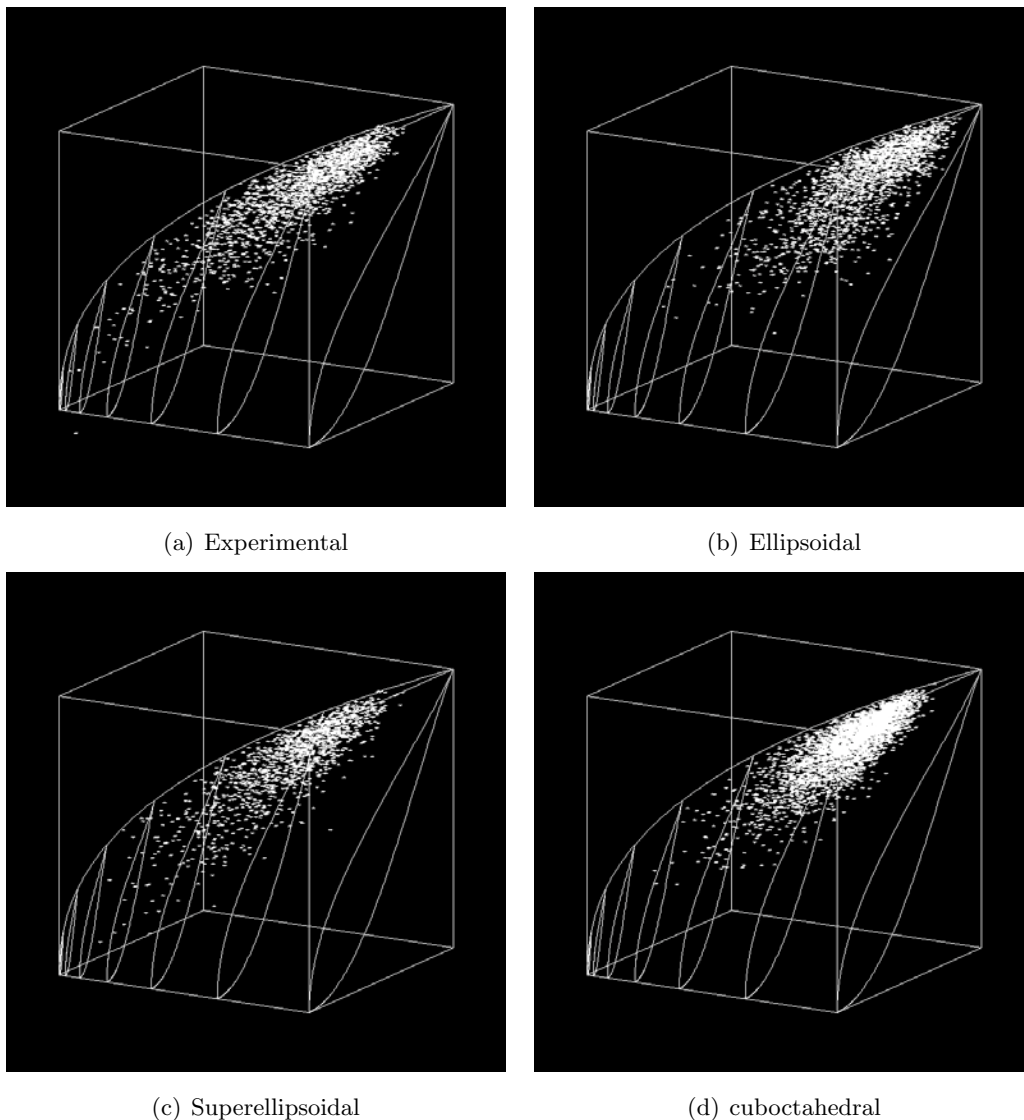


Figure XII: The plots of grains in moment invariant space for the (a) experimental, (b) ellipsoidal, (c) superellipsoidal, and (d) cuboctahedral datasets.

Another morphological descriptor that can be studied to understand shape complexity is the concavity. The statistics for the measure of concavity V/V_{conv} are given in Table 10. Remember that V/V_{conv} is a measure of concavity that equals 1 for a sphere, and as concavity increases, V/V_{conv} decreases. From Table 10, we can see that the ellipsoidal dataset is the most convex, followed by the cuboctahedral dataset, then the experimental dataset, and the least convex is

the superellipsoidal dataset. The ellipsoidal dataset is much more convex than the experimental dataset, while the cuboctahedral dataset matches experimental observations well with the median, but not well with the mean. The minimum V/V_{conv} values of the ellipsoidal and cuboctahedral datasets are about double the experimental observations, so the extreme values, which correspond to particularly concave and complex grains from the experimental dataset, are not being created in the ellipsoidal and cuboctahedral datasets. The superellipsoidal dataset, however, is more convex than the experimentally observed grains. The minimum, mean, and median are all lower in the superellipsoidal dataset than in the experimental dataset, so not only does the dataset have more concavity on average, its extreme values, or most concave grains, are more concave than the experimentally observed grains.

Statistic	Experimental	Ellipsoidal	Superellipsoidal	Cuboctahedral
Min	0.366	0.701	0.279	0.683
Max	0.984	0.999	0.979	0.984
Median	0.932	0.960	0.861	0.937
Mean	0.899	0.953	0.837	0.923
Std Dev	0.0879	0.0282	0.1097	0.0463

Table 10: The minimum, maximum, median, mean, and standard deviation of $V/V_{convexhull}$ for the experimental, ellipsoidal, superellipsoidal, and cuboctahedral datasets.

It is possible that morphological outliers due to segmentation errors affect the distribution of the experimental volume in ways which are difficult to reproduce. For example, if two grains are joined through segmentation errors, it is difficult and unrealistic to reproduce the combined grain using a single ellipsoid, superellipsoid, or cuboctahedron. It is likely, however, that we are using statistics generated from these badly segmented grains to generate our synthetic microstructures, so there will be a bias in the synthetic microstructures by trying to reproduce statistics that are incorrect to begin with. If this is the case, identification of those morphological outliers will be needed. We can identify those morphological outliers effectively using moment invariants.

Since $\bar{\Omega}_3$ decreases with increasing complexity, and we expect the morphological outliers to be complex, we can find morphological outliers by looking at the grains below some threshold value of $\bar{\Omega}_3$. The grains in the experimental dataset with $\bar{\Omega}_3$ less than two standard deviations below the mean $\bar{\Omega}_3$ are shown in Fig. XIII. We can see that there are some small grains that are morphological outliers, and also many large grains which are morphological outliers. Among them is the largest grain from the dataset. The large grains appear to mostly be where two or more grains have been joined together incorrectly due to segmentation errors. The mean $\bar{\Omega}_3$ of these grains is 0.2176. When they are removed from the dataset, the new mean is 0.6235, median is 0.6413, minimum is 0.3068, maximum is 0.8767, and standard deviation is 0.1262. Compare that with the old mean of 0.605 and it is apparent that the morphological outliers do have an effect on the dataset, not just

the extreme values.

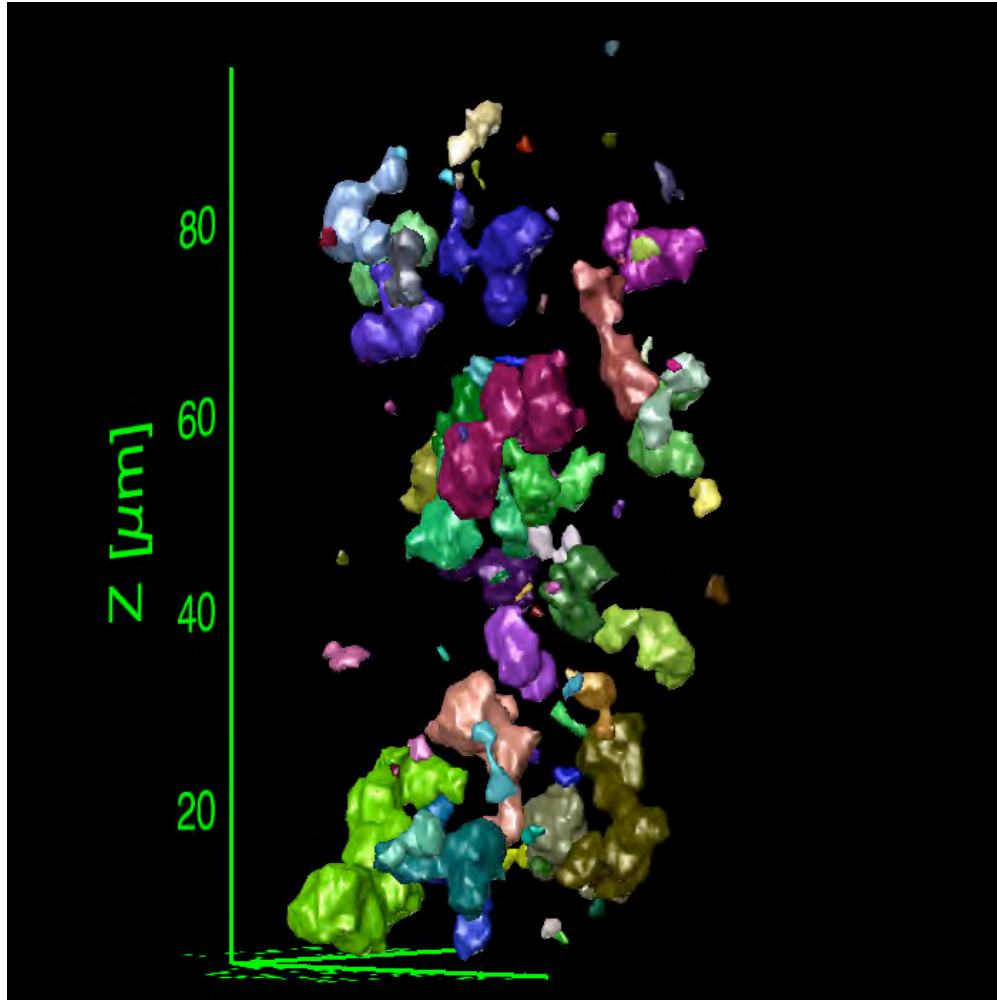


Figure XIII: A visualization of the grains in the experimental dataset with $\bar{\Omega}_3$ less than two standard deviations below the mean $\bar{\Omega}_3$.

It is a very complex task to reproduce real polycrystalline microstructures. There are different methods that can be used and tweaks that can be made to enhance the method of reproduction to match one descriptor, but it may have a negative effect on another descriptor. This is apparent when one considers the good matching of the superellipsoidal dataset to the experimentally observed grains for some descriptors, in moment invariant space for example, but then the poor matching of the measure of convexity V/V_{conv} . Steps should be taken to improve the segmentation of datasets that are used for the synthetic dataset generation so that artificial morphological outliers do not have a bad effect on the microstructure generation.

II Conclusions

We have applied the theory of 3-D moment invariants to a variety of shapes, including experimental serial sectioning data sets and synthetically generated microstructures. The method is easy to use, and allows for a quantitative description of shapes. Further applications of this approach are currently being considered, including extension to higher order moment invariants.

Bibliography

- [1] S.T. Wlodek, M. Kelly, and D.A. Alden. The structure of René-88 DT. In R.D. Kissinger, D.J. Deye, D.L. Anton, A.D. Cetel, M.V. Nathal, T.M. Pollock, and S.A. Woodford, editors, *Superalloys 1996*, pages 129–136, 1996.
- [2] L.J. Carroll, Q. Feng, J.F. Mansfield, and T.M. Pollock. Elemental partitioning in Ru-containing nickel-base single crystal superalloys. *Mat. Sci. Engg. A*, 457:292–299, 2007.
- [3] S. Ma, L.J. Carroll, and T.M. Pollock. Development of γ phase stacking faults during high temperature creep of Ru-containing single crystal superalloys. *Acta Mater.*, 55:5802–5812, 2007.
- [4] L.J. Carroll, Q. Feng, J.F. Mansfield, and T.M. Pollock. High refractory, low misfit Ru-containing single crystal superalloys. *Met. Mat. Trans A*, 37:2927–2938, 2006.
- [5] Q. Feng, L.J. Carroll, and T.M. Pollock. Solidification segregation in ruthenium-containing nickel-base superalloys. *Met. Mat. Trans A*, 37:1949–1962, 2006.
- [6] R.A. Lebensohn. N-site modeling of a 3D viscoplastic polycrystal using fast Fourier transform. *Acta Materialia*, 49:2723–2737, 2001.
- [7] D.T. Fullwood, S.R. Niezgoda, and S.R. Kalidindi. Microstructure reconstructions from 2-point statistics using phase-recovery algorithms. *Acta Materialia*, 56:942–948, 2008.
- [8] W.E. Lorenson and H.E. Cline. Marching cubes: a high resolution 3D surface reconstruction algorithm. *Computer Graphics*, 21:163–169, 1987.
- [9] Paraview. <http://www.paraview.org>.
- [10] J.P. MacSleyne, J.P. Simmons, and M. De Graef. On the use of moment invariants for the automated analysis of 3-D particle shapes. *Modeling and Simulations in Materials Science and Engineering*, 16:045008, 2008.
- [11] J. Ohser and F. Mücklich. *Statistical Analysis of Microstructures in Materials Science*. John Wiley and Sons Ltd., 2000.

- [12] J. Flusser, Suk T., and B. Zitová. *Moments and moment invariants in pattern recognition*. Wiley, 2010.
- [13] M. Novotni and R. Klein. Shape retrieval using 3D Zernike descriptors. *Computer Aided Design*, 36:1047–1062, 2004.
- [14] M. Groeber, S. Ghosh, M. D. Uchic, and M. Dimiduk. A framework for automated analysis and simulation of 3D polycrystalline microstructures. Part 1: Statistical characterization. *Acta Materialia*, 56:1257–1273, 2008.
- [15] M. Groeber, S. Ghosh, M. D. Uchic, and M. Dimiduk. A framework for automated analysis and simulation of 3D polycrystalline microstructures. Part2: Synthetic structure generation. *Acta. mater.*, 56:1274–1287, 2008.